Geophysical Research Letters

Supporting Information for

Multi-fault models of the 2019 Ridgecrest sequence highlight complementary slip and fault junction instability

Zhe Jia[1*], Xin Wang[1], Zhongwen Zhan[1]

[1] Seismological Laboratory, California Institute of Technology, Pasadena, CA 91125, USA.

Contents of this file

Introduction

This supporting information provides: three additional texts of methods (Text S1-S3), 12 figures (Figure S1-S13), and two tables (Table S1-S2), to support the main text.

Text S1. Calculation of 3D Green's function.

For the inversions of the near-field (epicentral distance within 100 km) observations, including 27 strong ground motion time series and 19 high-rate GPS traces, we adopt a 3D finite difference algorithm [*Graves*, 1996] to calculate 3D Green's functions, using the SCEC CVM-4.26 velocity model [*Small et al.*, 2017] as input. However, unlike 1D Green's functions that only depend on source-receiver distances and azimuths, 3D Green's functions have a nonlinear relationship with the source locations. Therefore, we need to calculate 3D Green's functions for all possible source locations for rupture inversions, and this can be highly computational consuming. To reduce the computational cost, we employed the strain Green's tensor and source-receiver reciprocity approach following Wang and Zhan [2020], in which we swap the locations of sources and receivers for the same elastic response [*Eisner and Clayton*, 2001; *Zhao et al.*, 2006]. In this way, each station is treated as a virtual seismic source. Thus the number of FD wavefield simulations is reduced to 47 (number of stations), which is much less than the number of sources (thousands of grids in the source region). We calculated 3D Green's functions with a grid spacing of 100 m, leading to the numerical accuracy of up to 0.5 Hz [*Wang and Zhan*, 2020]. We saved our Green's function database on a mesh of 2km*2km*1km for all 47 near-field stations. To reach source location resolution beyond the mesh precision, we interpolated the 3D Green's functions to all possible locations through a trilinear interpolation.

Text S2. Subevent inversions for the Mw 6.4 foreshock and Mw 7.1 mainshock.

We adopt subevent inversion for the rupture processes of the foreshock and mainshock. In this method, we decompose a large earthquake into a series of point source subevents, and simultaneously resolve their source parameters. Each subevent has 10 unknown parameters, including subevent locations (3), centroid times (1), source time durations (1), and deviatoric moment tensors (5). When the number of subevents n is large, resolving all $10*n$ unknown parameters through a purely nonlinear framework is inefficient. Therefore, we divide our inversion procedure into two stages, in which we nonlinearly optimize part of source parameters, while invert for other parameters in a linear framework.

In the outer stage, we search nonlinear parameters (subevent locations, centroid times and source durations) through Monte Carlo Markov chains (MCMC) with a Metropolis-Hasting algorithm. In each Markov Chain step, we propose new models through sampling one of the nonlinear parameters while keeping the other nonlinear parameter at their current values [*Bodin et al.*, 2012]. This approach ensures an overall high acceptance rate, and therefore improves the convergence efficiency of the MCMC inversion. Given the proposed nonlinear parameters in each MCMC step, we still need a set of subevent deviatoric moment tensors to calculate synthetic waveforms. These moment tensor components are linearly related to the observed time series and Green's functions [*Jost and Herrmann*, 1989], which allows an individual linear inversion of moment tensors when locations and timings of subevents are available. Therefore, we determine moment tensor components in the inner stage of each MCMC step. We first predict apparent source time functions (ASTFs) at all stations with corresponding nonlinear parameters, and then convolve these ASTFs with Green's functions. We further invert for deviatoric subevent moment tensors through extending the algorithm by Minson and Dreger [2008] to multiple point sources.

We generate 72 Markov Chains from random initial samples, and eventually keep 24 best fitting chains to avoid being trapped in local minima. The MCMC sampling follows a Bayesian framework, in which the prior probability density functions for all nonlinear parameters are bounded uniform distributions. We also introduce a penalty term to address the moment-duration scaling relationship of large earthquakes [*Meier et al.*, 2017], to reject subevent source time functions of highly inconsistent aspect ratios. Although the instrumental/noise errors of the seismic recordings are typically insignificant, additional errors can be caused by improper assumptions of the wave propagation processes (e.g. inaccurate velocity model, finite source effect, etc.). Therefore, we introduce data errors which are empirically set to be 10% of the final misfits between data and synthetics. These errors eventually propagate to subevent model errors. For both the foreshock and mainshock, we start with one subevent and iteratively increase the number of subevents, until the waveforms are well fitted and no significant subevent is missing for agreement with the long period seismic moment.

We use an assembly of near field strong ground motion traces (27 stations), teleseismic P waves (33 stations), and teleseismic SH waves (39 stations) in our subevent inversions. The weighting of these three datasets is set to 1:6000:800. This weighting scheme is consistent with the finite fault inversions in this study (Text S3), which leads to similar misfit contributions from different data types (Table. S3). Because it's usually difficult to precisely pick the first arrival times, we allow maximum time shifts of 3s, 2s, and 5s for the strong motion, P, and SH waves in our inversions, respectively. Since all traces can shift simultaneously, the absolute locations of all subevents can move together. To reduce this systematic error, we need to fix the location of one subevent while allowing other subevents to move freely in the whole space. Similar to Ross et al. [2019], we anchored the third subevent for the Mw 6.4 foreshock at an arbitrarily selected maximum surface

offset point on the southwest striking fault plane. For the Mw 7.1 mainshock, we fixed the last subevent at the location near the southeastern end of the major fault, where a slip patch is observed from various slip inversions [*Barnhart et al.*, 2019; *Liu et al.*, 2019; *Ross et al.*, 2019]. Reliabilities of the subevent locations for the foreshock and mainshock are assessed by the Markov Chain ensemble distributions in Fig. S3 and Fig. S10, respectively.

Text S3. Finite fault inversions.

We estimated the minimum number of necessary fault segments for both the foreshock and mainshock by analyzing whether each subevent pair of an earthquake can be put on the same fault plane, given their locations and strike/dip angles. The nodal plane ambiguities are resolved with help from the spatial temporal evolution of subevents. Each fault segment goes through the location of these subevents, and their strike/dip/rake angles are consistent with the corresponding subevent focal mechanisms. The maximum fault depth is 16 km. We discretized each fault segment into subfault grids which horizontal and depth intervals are both 2 km. These subfault grids have triangle moment rate functions with a duration of 2s. Given the rupture directivity estimated from the subevent model, we assume that the rupture starts from a subfault grid of the same depth as the corresponding subevent, and the initiation point locates at one edge of the whole fault segment. We then tracked the rupture initiation time back from the subevent centroid time using a rupture velocity either approximated from subevent centroidal velocity or from grid-search. We further generated rupture contours and calculated the rupture time for each subfault grid.

For the Mw 6.4 foreshock, we constructed two fault segments that are nearly orthogonal. The NW trending segment has a strike of 320° and dip of 80°. The SW striking segment has a strike of 228° and dip of 90°. The rupture initiation depths of the NW- and SW- trending faults are 9 km and 5 km, respectively. The subevent E2 of the foreshock may reflect slip on both NW- and SW- trending fault segments. Thus the estimation of subevent centroidal rupture velocity based on E2-E3 can be biased. Instead, we find an optimal rupture velocity of 2.0 km/s through a grid-search (Fig. S5). For the Mw 7.1 mainshock, we constructed two major fault segments F1 (strike/dip: 320°/90°) and F2 (strike/dip: 320°/80°), and a shallower subparallel fault branch F3 (strike/dip: 329°/70°), to reconcile the steep (68°) dip angle of subevent E3 and the curved surface rupture traces (Fig. 1A). We use a rupture velocity of 1.7 km/s approximated from centroidal velocity from subevent E3 and E5.

Once we set up the fault geometries, focal mechanisms, and rupture times, we only have slip amplitudes as unknown parameters. Here we use a linearized finite fault inversion method of Hartzell and Heaton [1983] to determine the slip distributions. In this framework, the observed data and the subfault synthetics form a linear system,

$$\begin{bmatrix} G_{SM}^{1} & G_{SM}^{2} & \cdots & G_{SM}^{n} \\ G_{TelPdisp}^{1} & G_{TelPdisp}^{2} & \cdots & G_{TelPdisp}^{n} \\ G_{TelPvel}^{1} & G_{TelPvel}^{2} & \cdots & G_{TelPvel}^{n} \\ G_{TelSHdisp}^{1} & G_{TelSHdisp}^{2} & \cdots & G_{TelSHdisp}^{n} \\ G_{HRGPS}^{1} & G_{HRGPS}^{2} & \cdots & G_{HRGPS}^{n} \\ G_{InSAR}^{1} & G_{InSAR}^{2} & \cdots & G_{InSAR}^{n} \end{bmatrix} * \begin{bmatrix} m^{1} \\ m^{2} \\ \vdots \\ m^{n} \end{bmatrix} = \begin{bmatrix} d_{SM} \\ d_{TelPdisp} \\ d_{TelPvel} \\ d_{TelSHdisp} \\ d_{HRGPS} \\ d_{InSAR} \end{bmatrix}$$

in which $m^{1\cdots n}$ is the slip vector of all subfault grids, $d_{[data\ type]}$ is the data vector including a variety of data types (Strong motion, teleseismic P waves in displacement, teleseismic P waves in velocity, teleseismic SH waves in displacement, high-rate GPS and InSAR). $G_{[data\ type]}^{1\cdots n}$ are the synthetics of different data types for unit slip on subfault grids from 1 to *n*. For the seismic and HRGPS data, both $G_{[data\ type]}^{1\cdots n}$ and $d_{[data\ type]}$ are stringing time series of all stations from end to end. For the InSAR data, data and Green's functions are formatted as gridded surface line-of-sight (LOS) displacements. Therefore, all time points of seismic and HRGPS records, and all discrete displacements of the InSAR data are included in the inversion.

The slip can be directly resolved with a least square solution, but the result is unstable because this inverse problem is usually ill-posed. To stabilize the inversion, we introduce four types of constraints, including 1) non-negative constraints on the slip, 2) minimization of the slip differences between adjacent subfault grids, 3) penalizing slip at the non-surface boundaries of the faults, and 4) minimizing the L2 norm of the slip distribution [*Hartzell and Heaton*, 1986; *Ji et al.*, 2002]. These constraints allow us to reject unphysical solutions (negative slip, enormous strain, etc.) and avoid overfitting. To flexibly incorporate these constraints, we solved the inverse problem through the CVX optimization algorithm [*Grant and Boyd*, 2014]. The slip uncertainties are estimated using a cut-half Jackknifing approach in which we randomly remove half of all data points and run the slip inversion. We repeated this process 100 times, and then calculated the standard deviation of the obtained slip models for an approximation of the model error (Fig. S7, S13).

Compared with the subevent inversions, we added time series of 19 high-rate GPS stations (low-passed to 0.2 Hz) and InSAR line-of-sight (LOS) measurements from the ALOS-2 and Sentinel-1 satellites in the finite fault inversions. The weighting of regional strong ground motion, teleseismic P waves, teleseismic SH waves, high-rate GPS time series and InSAR LOS displacements in our slip inversions is 1:6000:800:0.25:10. This weighting scheme results in comparable misfit contributions of the different datasets (Table S3), and insignificant changes of the weightings don't substantially alter the inversion results. For the high-rate GPS data, we didn't use the vertical component time series in our inversions due to their low signal-to-noise ratio. Instead, we forward predicted the synthetics of vertical component HRGPS and compared them with the data (Fig. 2, 3; Fig. S6, S12). The InSAR data spans over both the Mw 6.4 foreshock and the Mw 7.1 mainshock, forming a trade-off in resolving slip distributions of these events. Considering the foreshock causes much less surface deformation than the mainshock, we excluded the InSAR data from the foreshock slip inversion. Using the foreshock slip model derived from other datasets, we forward calculated its LOS displacements, and assume this as the data contribution from the foreshock. We then subtracted the InSAR data by the foreshock LOS displacements, and attributed the residuals as InSAR data for being incorporated in the mainshock slip inversion.

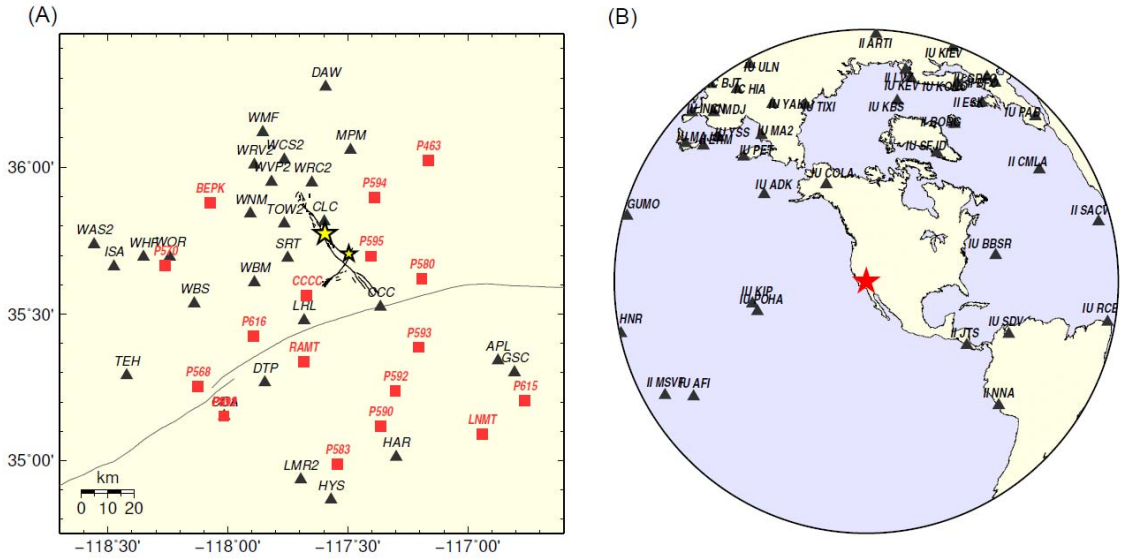

Figure S1. Seismic and GPS stations used in this study. (A) Distribution of the 27 near field strong motion stations (black triangles) and 19 high-rate GPS stations (red squares). The yellow stars indicate the hypocenter of the Mw 6.4 foreshock and Mw 7.1 mainshock. The black and gray lines delineate the Ridgecrest and Garlock faults in Fig. 1. (B) Distribution of 39 teleseismic stations (black triangles) used in this study. The red star shows the hypocenter of the Mw 7.1 mainshock.

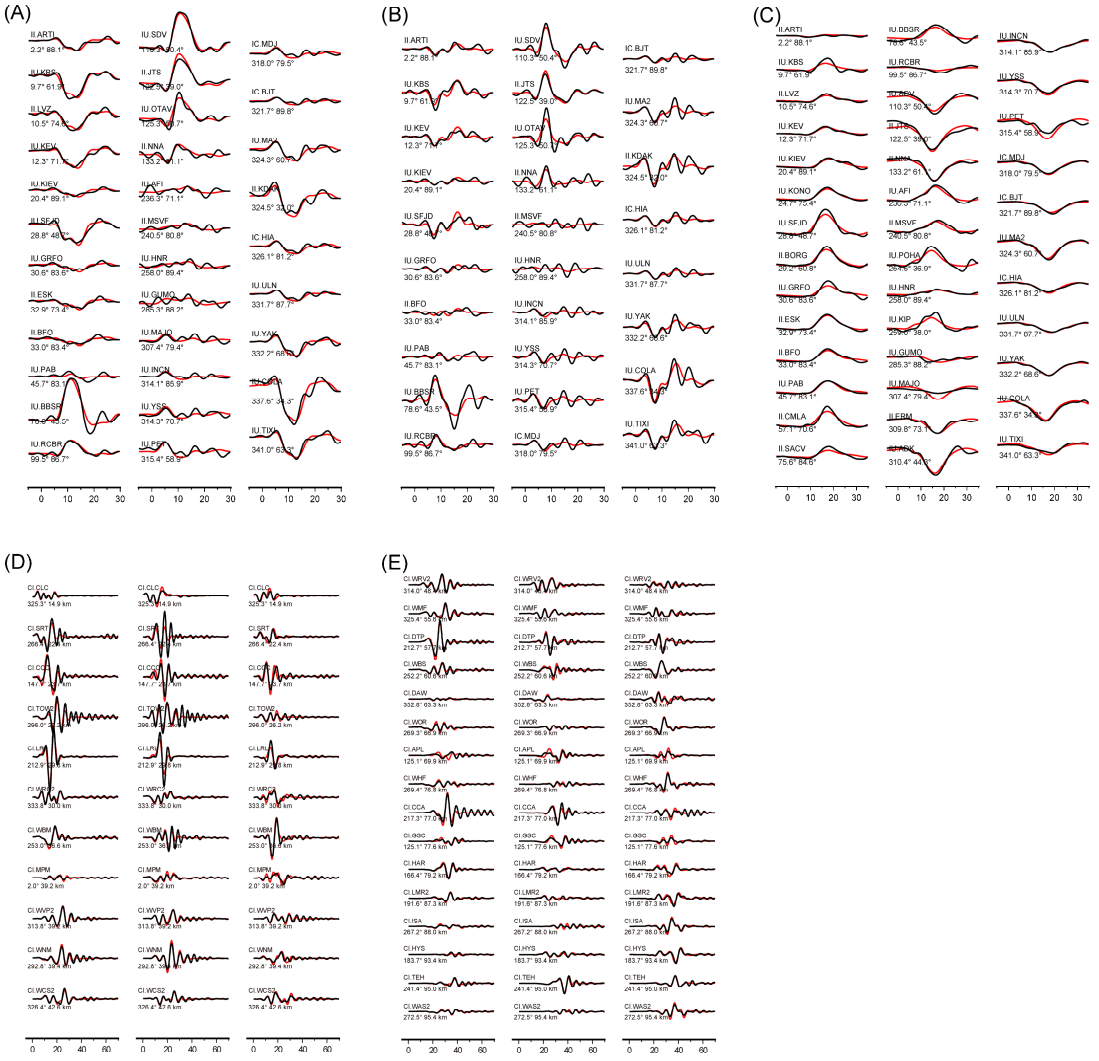

Figure S2. Waveform fits for the preferred subevent model of the Mw 6.4 foreshock. Black and red lines indicate data and synthetic waveforms, respectively. The numbers below each trace show the station azimuth and distance, respectively. (A) P waves in displacement. (B) P waves in velocity. (C) SH waves in displacement. (D-E) Near field strong ground motion waveforms.

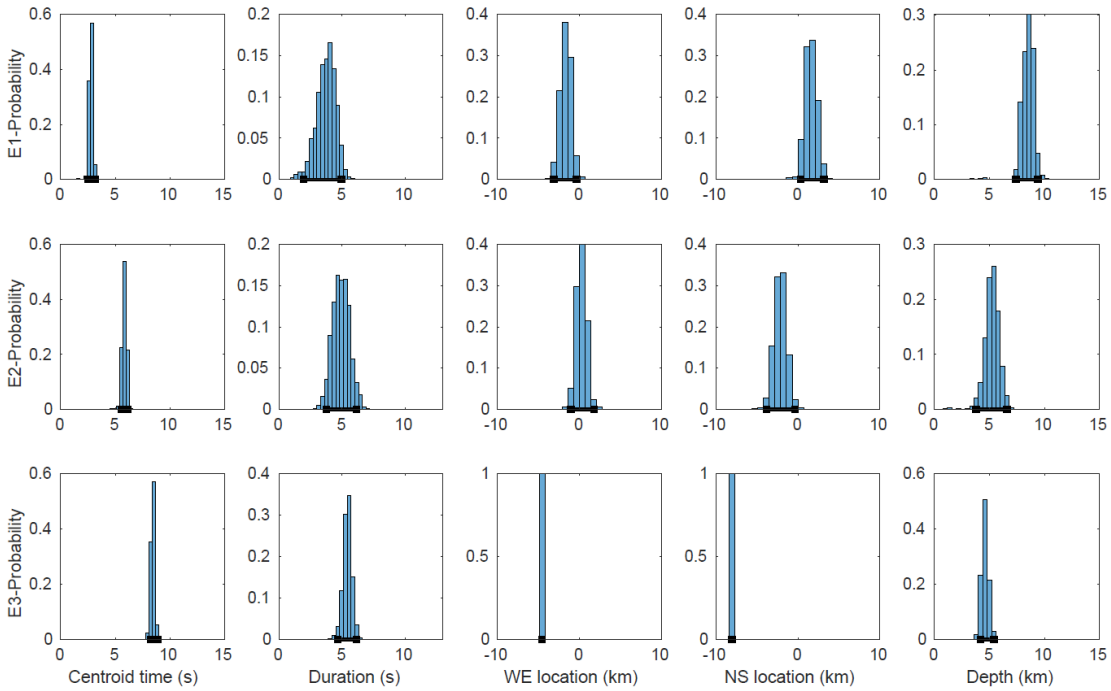

Figure S3. Distributions of Markov Chain samples in the subevent inversion of the Mw 6.4 foreshock. Columns from left to right show the density distribution of subevent centroid times, durations, west-east locations, north-south locations and centroid depths. Rows indicate subevent E1-E3. Black squares and lines denote error bars corresponding to 95 % confidential interval.

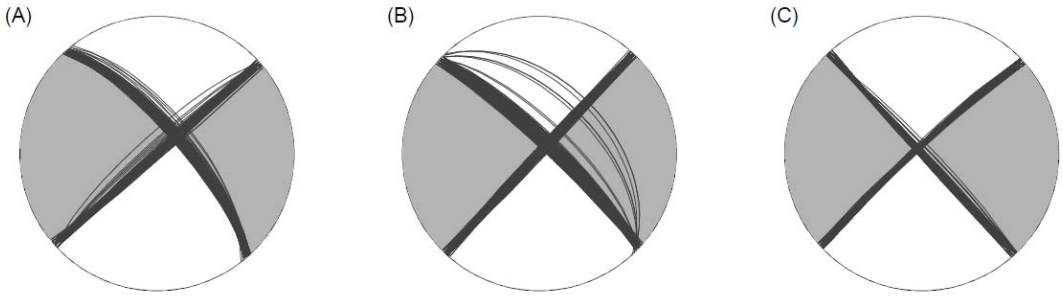

Figure S4. Scatters of double couple focal mechanisms for subevent E1 (A), E2 (B) and E3 (C) of the Mw 6.4 foreshock.

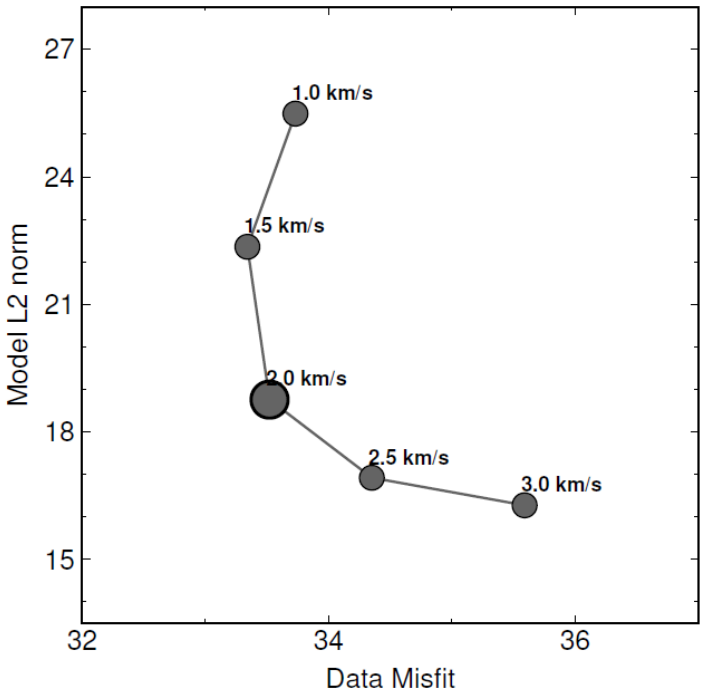

Figure S5. Grid-search of the rupture velocity for the Mw 6.4 foreshock slip inversions. When the rupture velocity is 2.0 km/s, both the data misfit and L2 norm of the slip model are low.

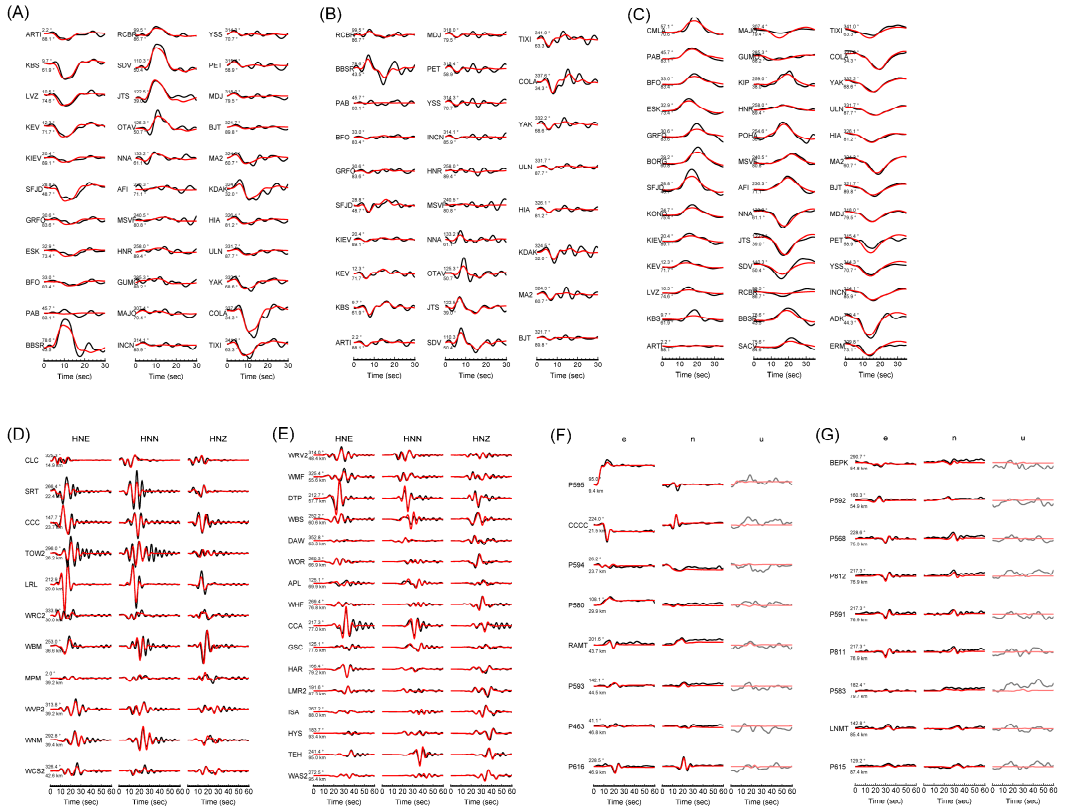

Figure S6. Waveform fits for the preferred 2-fault slip model of the Mw 6.4 foreshock. Black and red lines indicate data and synthetic waveforms, respectively. The numbers leading the waveforms are the azimuths and epicentral distances. (A) P waves in displacement. (B) P waves in velocity. (C) SH waves in displacement. (D-E) Near field strong ground motion waveforms. (F-G) Near-field HRGPS time series. The U-D component of the HRGPS data, as shown in lighter colors, are not used in the inversion.

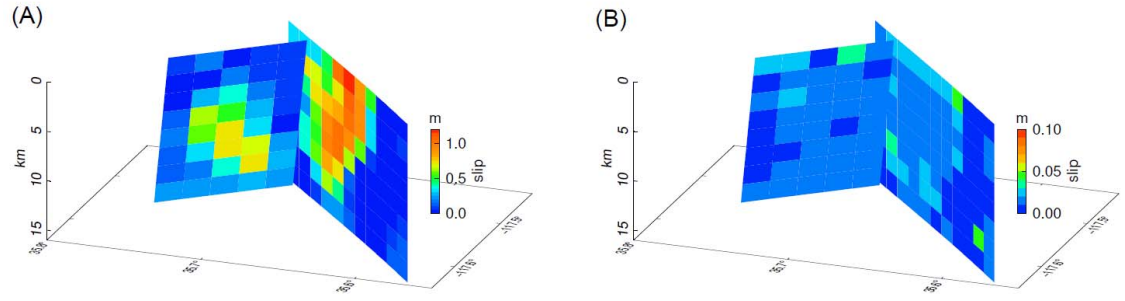

Figure S7. Assessment of model error with the Jackknifing test for the Mw 6.4 foreshock. (A) Slip distribution. (B) Standard deviation.

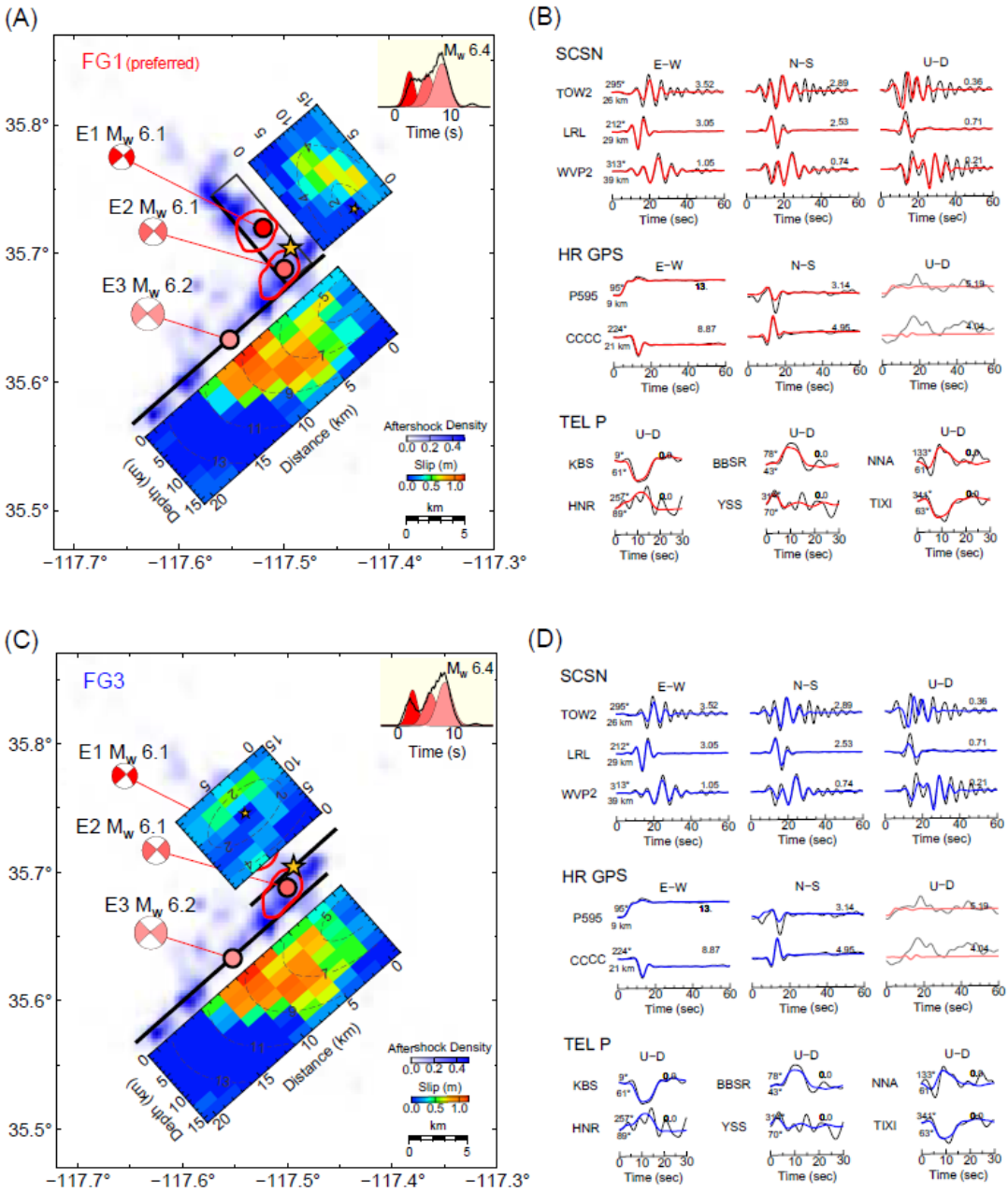

Figure S8. Same as Fig. 2 but for the comparison between conjugate fault model FG1 (A-B) and parallel fault model FG3 (C-D). The synthetics from FG1 fits the N-S and U-D components of stations TOW2 and WVP2 better than FG3.

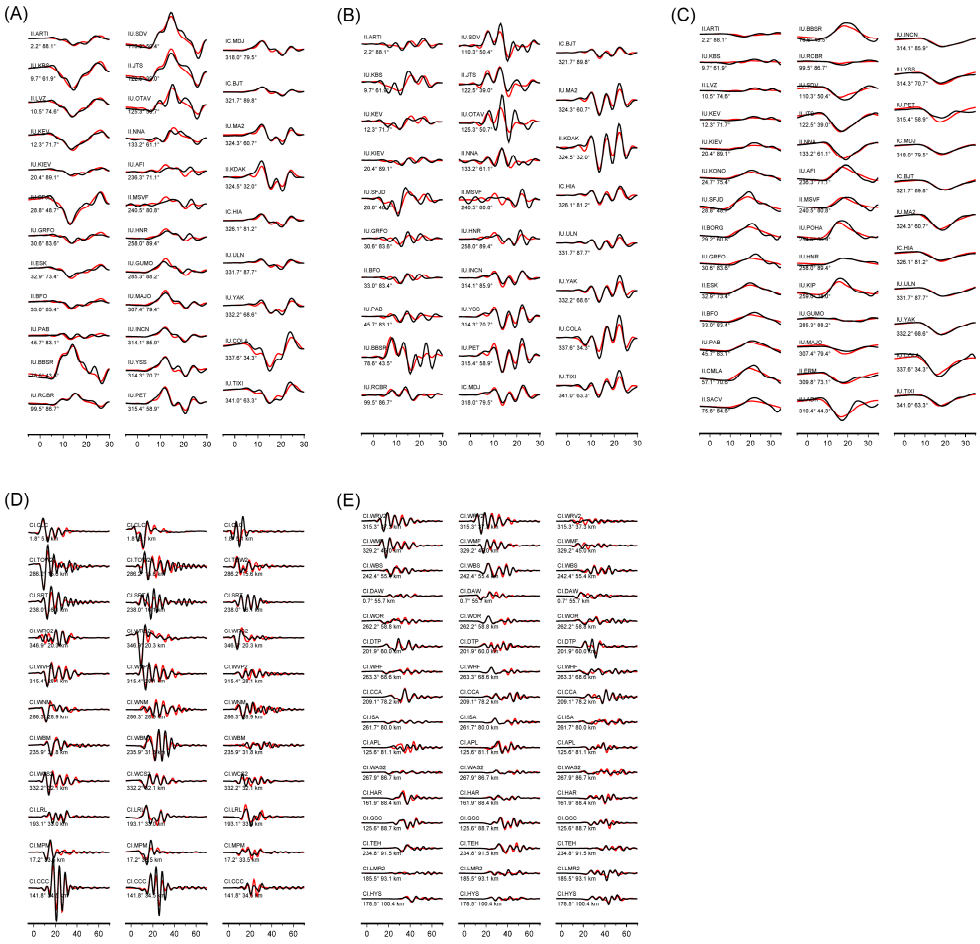

Figure S9. Same as Fig. S2 but for the Mw 7.1 mainshock.

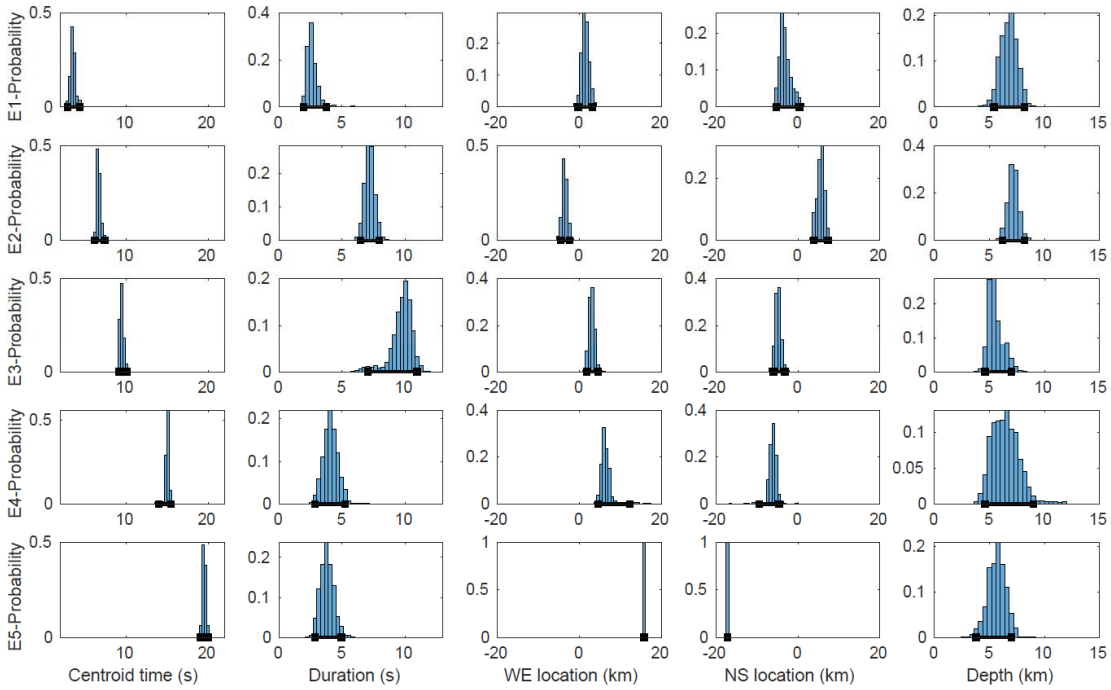

Figure S10. Same as Fig. S3 but for the Mw 7.1 mainshock.

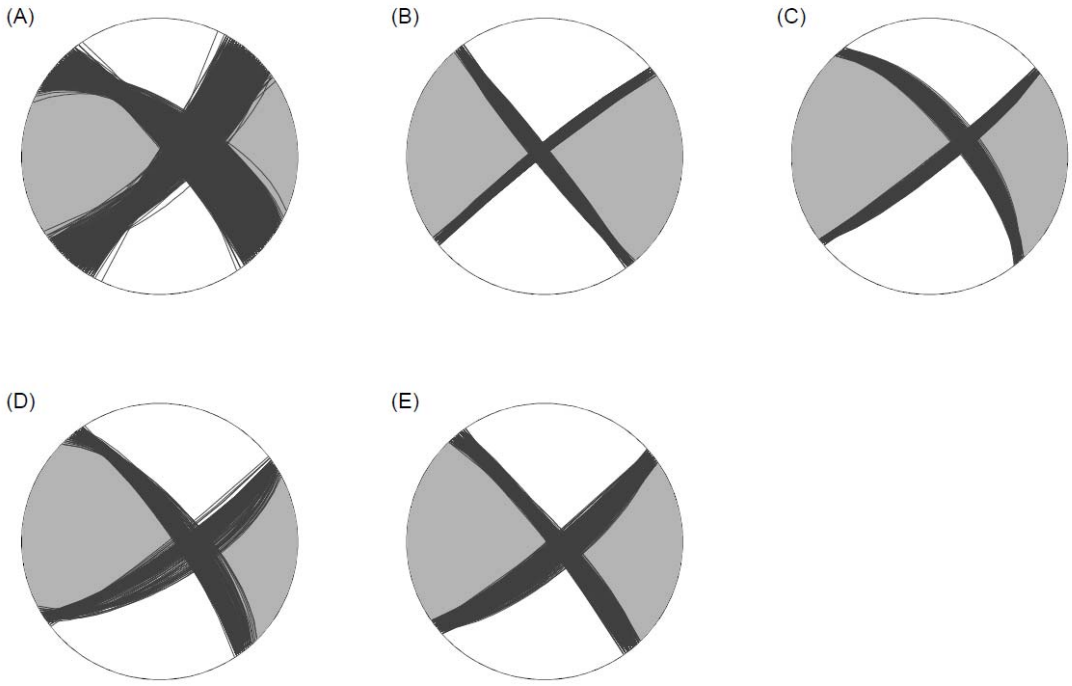

Figure S11. Same as Fig. S4 but for the Mw 7.1 mainshock.

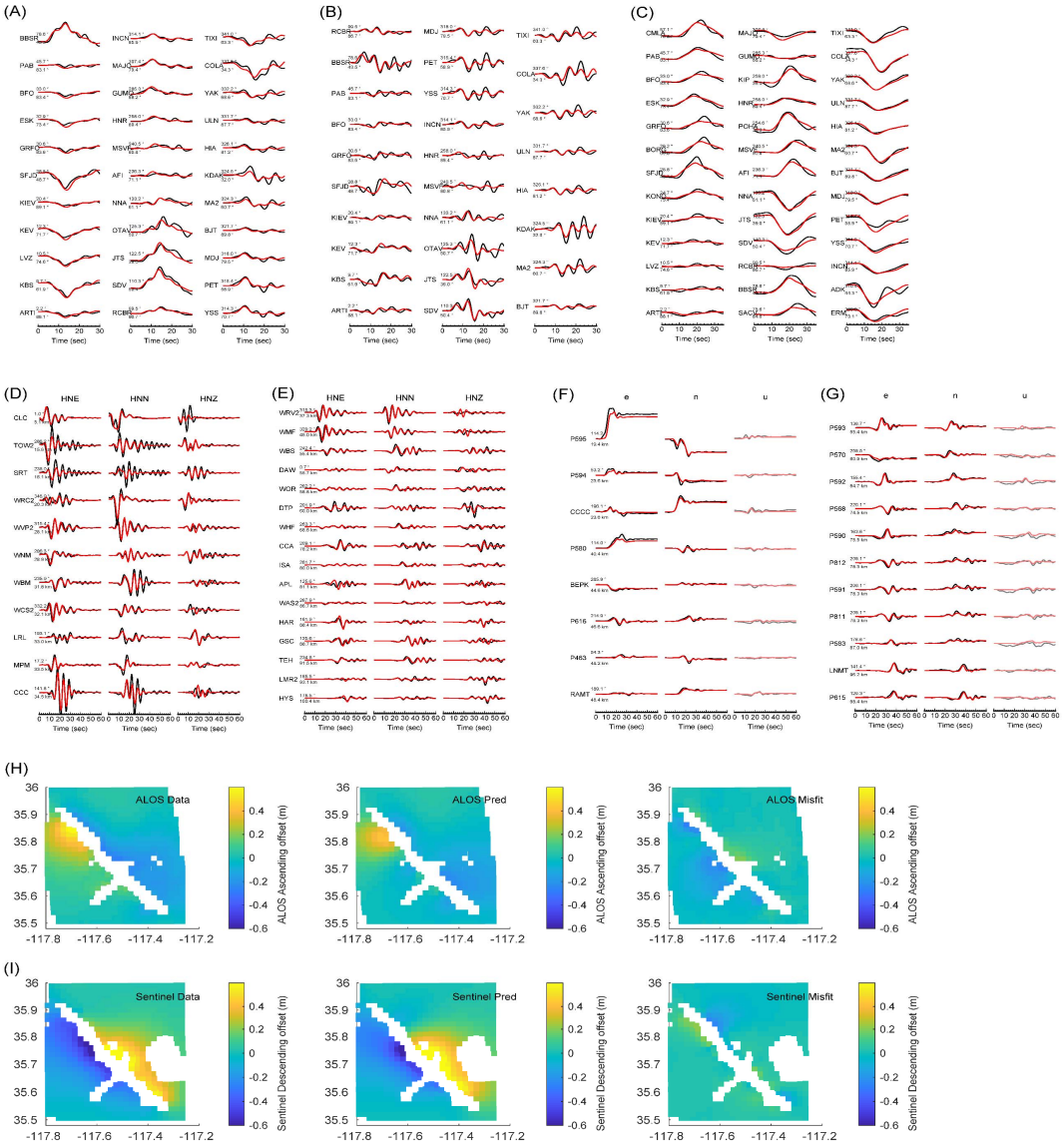

Figure S12. Data fittings for the preferred slip model of the Mw 7.1 mainshock. (A-G) Same as Fig. S6 but for the Mw 7.1 mainshock. (H-I) Fittings of InSAR LOS displacements for the ALOS-1 ascending and Sentinel-2 descending tracks, respectively.

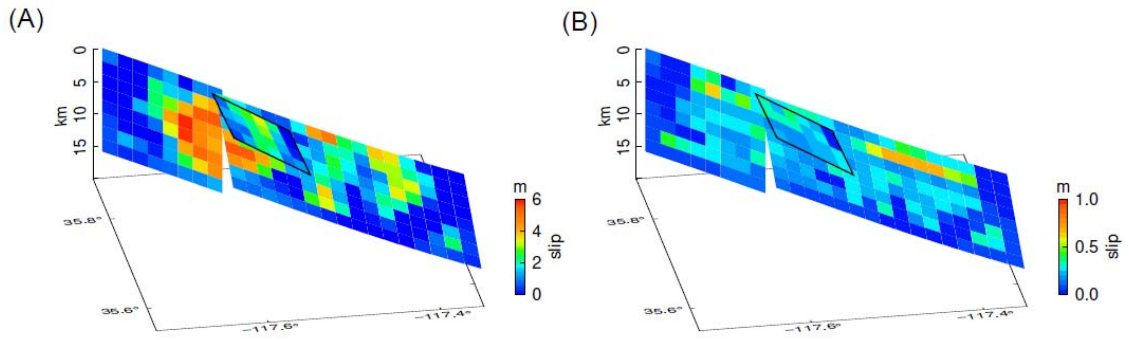

Figure S13. Same as Fig. S7 but for the Mw 7.1 mainshock.

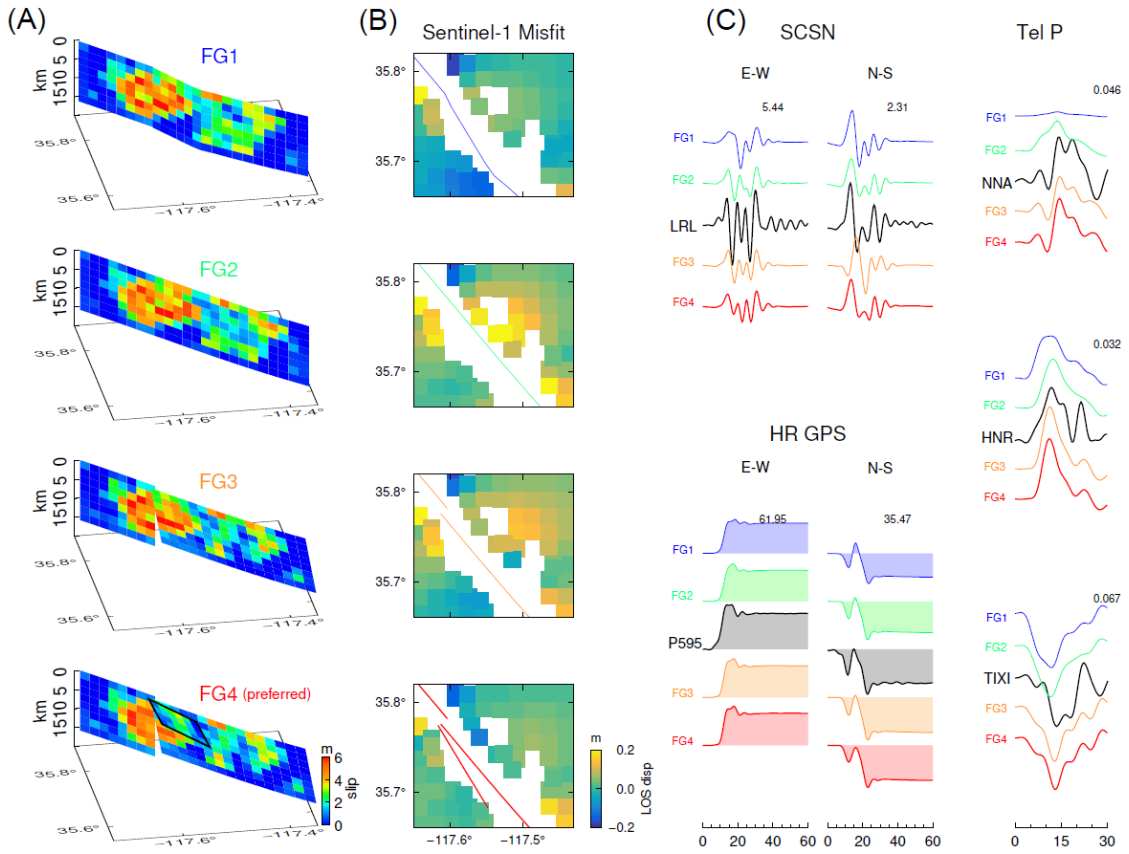

Figure S14. Comparison of 4 finite fault slip models for the Mw 7.1 mainshock assuming different fault geometries. (A) Slip distributions inferred from four fault geometries FG1-FG4, in which FG4 is preferred in this study (same as Fig. 3A). (B) Sentinel-1 InSAR displacement misfits for four geometrical settings. Solid lines in blue, green, orange and red show the fault surfaces for the corresponding models FG1-4, respectively. (C) Comparison of strong ground motion (SCSN), HRGPS and Telseismic P waveforms. Data is shown in black, and synthetics for models FG1-FG4 are indicated by blue, green, orange and red traces, respectively.

	Centroid time (s)	Duration (s)	Longitude (°)	Latitude (°)	Depth (km)	Mrr (10^{26} dyne-cm)	Mtt (10^{26} dyne-cm)	Mpp (10^{26} dyne-cm)	Mrt (10^{26} dyne-cm)	Mrp (10^{26} dyne-cm)	Mtp (10^{26} dyne-cm)
E1	2.64	3.61	-117.520	35.720	8.90	0.000	-0.143	0.142	0.027	0.025	0.018
E2	5.79	4.81	-117.500	35.688	5.81	0.000	-0.179	0.180	0.012	0.014	-0.014
E3	8.43	5.57	-117.552	35.633	4.42	0.006	-0.279	0.272	0.011	-0.014	0.024

Table S1. Subevent model parameters for the M 6.4 foreshock.

	Centroid time (s)	Duration (s)	Longitude (°)	Latitude (°)	Depth (km)	Mrr (10^{26} dyne-cm)	Mtt (10^{26} dyne-cm)	Mpp (10^{26} dyne-cm)	Mrt (10^{26} dyne-cm)	Mrp (10^{26} dyne-cm)	Mtp (10^{26} dyne-cm)
E1	3.78	2.26	-117.582	35.745	6.49	-0.007	-0.163	0.169	0.009	0.080	-0.021
E2	6.68	7.08	-117.640	35.813	7.30	0.001	-1.534	1.533	0.035	-0.144	0.391
E3	9.58	9.52	-117.564	35.724	5.03	0.067	-1.762	1.696	0.423	0.594	0.332
E4	15.15	4.34	-117.538	35.704	5.89	0.109	-0.638	0.529	0.023	0.145	0.222
E5	19.51	5.83	-117.422	35.614	5.83	0.004	-0.465	0.461	-0.001	0.085	0.083

Table S2. Subevent model parameters for the M 7.1 mainshock.

	Total misfit	Strong motion	Tel P	Tel SH	HR GPS	InSAR
Mw 6.4	33.5	19.4	18.8	11.7	16.1	NaN
Mw 7.1	141.1	80.1	56.4	42.8	30.6	27.1

Table S3. Contributions to misfit from different data types in the finite fault inversions.